PHYSICAL REVIEW E **99**, 053207 (2019)

Interpretation of proton radiography experiments of hohlraums with three-dimensional simulations

P.-E. Masson-Laborde,[1] S. Laffite,[1] C. K. Li,[2] S. C. Wilks,[3] R. Riquier,[1] R. D. Petrasso,[2] G. Kluth,[1] and V. Tassin[1]
[1]*CEA, DAM, DIF, F-91297 Arpajon Cedex, France*
[2]*Plasma Science and Fusion Center, Massachusetts Institute of Technology, Cambridge, Massachusetts 02139, USA*
[3]*Lawrence Livermore National Laboratory, 7000 East Avenue, Livermore, California 94550, USA*

(Received 10 July 2018; revised manuscript received 5 February 2019; published 28 May 2019)

Proton radiography experiments of laser-irradiated hohlraums performed at the OMEGA laser facility are analyzed using three-dimensional (3D) hydrodynamic simulations coupled to a proton trajectography package. Experiments with three different laser irradiation patterns were performed, and each produced a distinct proton image. By comparing these results with synthetic proton images obtained by sending protons through plasma profiles in the hohlraum obtained from 3D radiation hydrodynamic simulations, it is found that the simulated images agree favorably with the experimental images when electric fields, due to the electron pressure gradients that arise from 3D structures occurring during plasma expansion, are included. These comparisons provide quantitative estimates of the electric field present inside the hohlraums.

DOI: 10.1103/PhysRevE.99.053207

I. INTRODUCTION

In the context of indirect drive inertial confinement fusion (ICF) [1], a hohlraum, defined as a high-Z radiation enclosure, is used to convert the incident laser energy to x rays in order to compress a microsphere of fuel (the capsule) placed at its center. Hohlraums have also been used to create high-energy density (HED) plasma conditions for laboratory astrophysics experiments [2,3].

Electric fields E and magnetic fields B can be generated by many processes inside the hohlraum. From the generalized Ohm's law, the electric field E is given by

$$\boldsymbol{E} = -\frac{\nabla p_e}{e n_e} - \frac{\bar{\bar{\beta}} \cdot \nabla T_e}{e} - \boldsymbol{v} \times \boldsymbol{B} + \frac{\bar{\bar{\alpha}} \cdot \nabla \times \boldsymbol{B}}{\mu_0} + \frac{(\nabla \times \boldsymbol{B}) \times \boldsymbol{B}}{e n_e \mu_0}. \tag{1}$$

With e the electron charge, p_e the electron pressure, T_e the electron temperature, n_e the electron density, $\bar{\bar{\beta}}$ the thermoelectric conductivity tensor, $\mathbf{v}$ the plasma fluid velocity, μ_0 the magnetic constant, and $\bar{\bar{\alpha}}$ the electric resistivity. The B field is given by the Faraday's law $\frac{\partial \boldsymbol{B}}{\partial t} = -\nabla \times \boldsymbol{E}$.

The first two terms in Eq. (1) are, respectively, the thermoelectric source term (from the electron pressure gradient) and the Nernst source term. The last three terms related to the B field are, respectively, the advection of the magnetic field by the fluid, the resistive diffusion, and the Hall source term. The E-field generation is dominated by the electron pressure gradient [4], and the B-field generation by the noncollinear electron density and temperature gradients (Biermann battery effect) [5–7].

The presence of electric and magnetic fields can affect the plasma dynamics inside the hohlraum. B fields can affect electron thermal transport by changing thermal conductivity [6], while E fields play an important role in the inhibition of electron heat flux, through mechanisms like the return current instability [8,9].

Over the years, proton radiography has been successful in producing detailed images of protons being deflected and scattered as they transit through hohlraums. Indeed, this method is sensitive to density and to E and B fields. These images are formed by ballistic protons that propagate through the plasma present inside a hohlraum, ultimately being collected by a detector. As they transit the hohlraum, they are either deflected by the Lorentz force associated with the fields or scattered in the plasma (or wall), before being detected. Thus, the deflections induced in the proton trajectories are a direct measure of the E and B fields present inside the hohlraum [10,11]. The proton fluence on the detector is a quantitative measure of this deflection.

Laser-driven implosions of D ^{3}He capsules produce a monoenergetic proton source at 3 MeV (through the reaction $D + D \rightarrow T + p$) and 14.7 MeV (through the reaction $D + {}^3H_e \rightarrow \alpha + p$) [12,13]. Because this source produces a short burst of protons ($\approx$100 ps) the resulting images perform instantaneous snapshots of the fields, since the plasma in the hohlraum develops on the nanosecond timescale. This method of proton imaging has been extensively used to study ICF implosions [12–16], hydrodynamic instabilities and plasma flows in hohlraums [17,18], the existence of electromagnetic fields in hohlraums [19,20], planar plastic foils [21,22], and imploding capsules [23]. Laser propagation and filamentation in hohlraums for conditions relevant to ICF have also been studied by proton radiography [24–26].

In this article, we present an interpretation of proton radiography experiments through comparisons with combined three-dimensional (3D) hydrodynamics and proton ray-tracing simulations. This modeling predicts that 3D effects occurring during early-time plasma-wall expansion inside vacuum hohlraums give rise to specific geometry and values of the E field ($\simeq 10^8$ V/m) in the hohlraum that are then observed as variations in proton fluence on a synthetic proton radiograph. These images are then compared to detector images obtained in the proton radiographs. By comparing the two images, we find that the field generation is due to

2470-0045/2019/99(5)/053207(5)

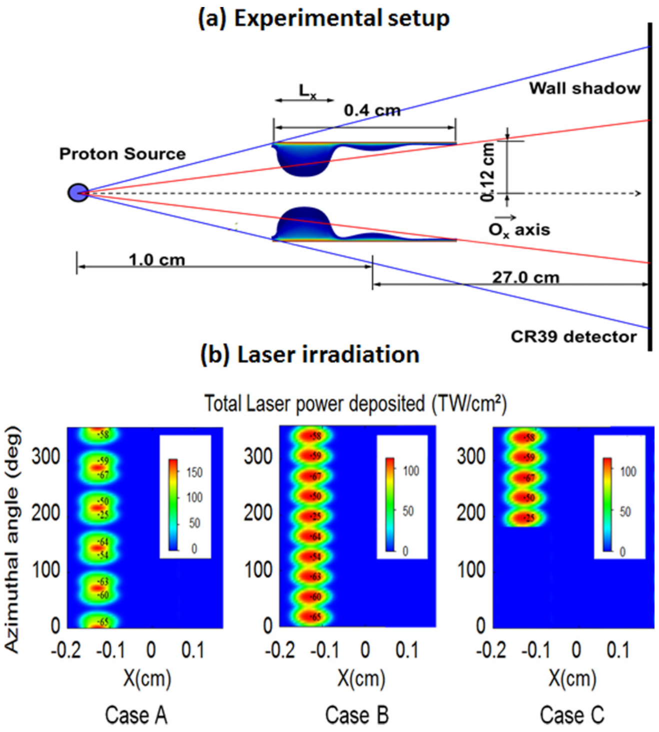

FIG. 1. (a) Experimental setup showing source protons going through the hohlraum and imaged on the detector. Red (solid) and blue (dashed) lines correspond to the geometrical limitation induced by the laser entrance holes (LEHs) of the hohlraums. (b) Laser irradiation used in the experiment: Case A (10 beams grouped by two), Case B (10 beams uniformly spaced), and Case C (five beams uniformly spaced on one side of the hohlraum).

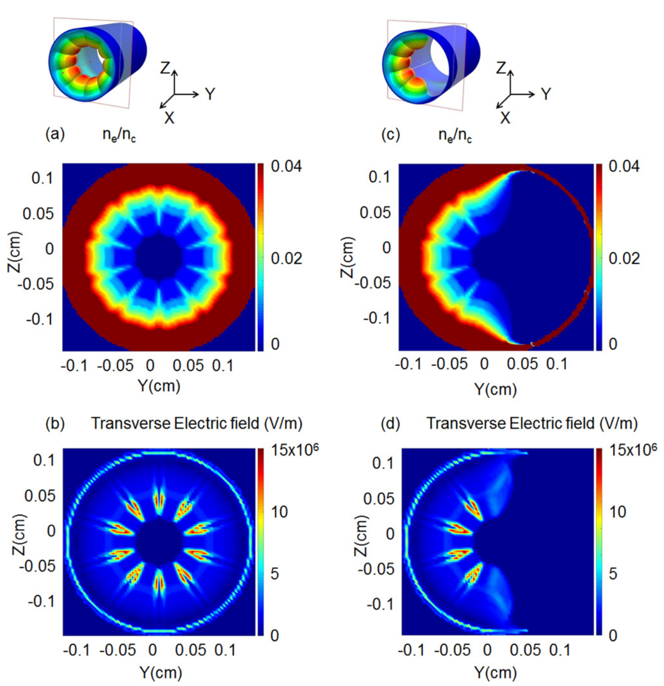

FIG. 2. 2D maps of electron density n_e/n_c [(a)–(c)] and transverse electric field $|\boldsymbol{E}_\perp|$ in V/m [(b)–(d)] taken at $t = 1.3$ ns from 3D simulations, at $x = 0.12$ cm along the hohlraum axis. Panels (a) and (b) are for Case B, (c) and (d) for Case C.

high-density gradients of plasma located between each of the plasma plumes created by laser beams incident on the hohlraum wall.

II. EXPERIMENTS AND DISCUSSION

A. Experiments

The experiments, illustrated in Fig. 1(a), were performed at the OMEGA laser facility [27]. A proton backlighter (D ^{3}He capsule) located 1 cm from the hohlraum center is imploded to generate the proton isotropic source. The hohlraums are vacuum hohlraums with a gold or CH wall in one of three laser configurations: Case A (10 beams grouped by two), Case B (10 uniformly spaced beams), or Case C (five uniformly spaced beams) as shown in Fig. 1(b). Each beam comes in at 59° to the hohlraum axis with a wavelength of 0.351 μm and energy ∼500 J in a 1 ns square pulse. Case A is the actual laser irradiation that has been used in the past OMEGA experiments [18,19,28], whereas Cases B and C are simple designs to simplify direct comparison to 3D simulations.

B. Hydrodynamic simulations

To analyze these different configurations, 3D radiative hydrodynamic simulations have been carried out with the 3D code Troll at CEA [29]. This code is a radiative hydrodynamic code, Lagrangian with the possibility of an arbitrary Lagrangian Eulerian (ALE) method with unstructured meshes. Radiative transport, laser absorption, and nonlocal thermodynamic equilibrium (NLTE) atomic physics are included. Thermal conduction can be treated either as a flux limiter or with a nonlocal model from Shurtz, Nicolai, and Busquet's multigroup diffusion model [30]. Cases B and C are shown for a gold hohlraum in Fig. 2. The electron density n_e/n_c is illustrated for a transverse cut (y, z) located in the middle on the expanding plasma along the longitudinal direction (axis hohlraum) at position $x = 0.12$ cm. During the plasma blowoff the plasma plumes expand and before stagnation on axis, and this expansion leads to high-density regions between them, as can be seen in Figs. 2(a) and 2(c). In Case C, the top and bottom plumes do not have neighbors on their sides, so no overdense plasma regions can be seen.

The direction of the electron pressure gradient is such that it leads to a lateral electric field pointing away from the region between each plasma plume, as was suggested before [18] but never confirmed by calculations. This transverse electric field $|\boldsymbol{E}_\perp| \equiv \sqrt{E_y^2 + E_z^2}$ (in V/m) is illustrated in Figs. 2(b) and 2(d). This indicates that the largest field is located between the plasma bubbles and can reach values close to 15 (50) MV/m for the gold (CH) hohlraum.

As the electric field is calculated from the electron pressure gradient between the expanding plasma plumes, its maximum value has a strong dependency on the mesh refinement used in the calculation. Two-dimensional (2) well-resolved plane simulations have been conducted, allowing better resolution than in three dimensions, with a mesh resolution of 1 nm in the radial direction (compared to 5 nm in three dimensions, laser direction) and variation of the transverse cell size. In

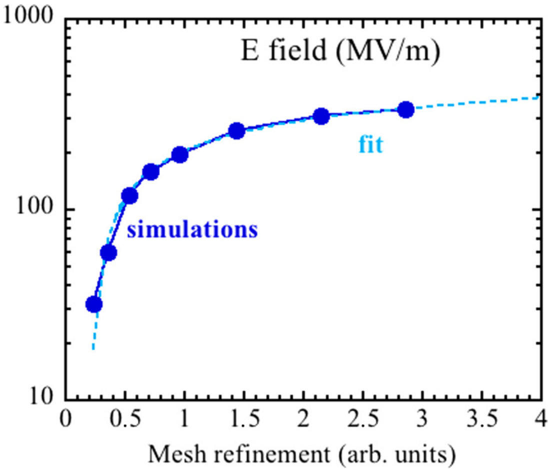

FIG. 3. Transverse electric field (in MV/m) from 2D plane simulations as a function of the mesh refinement in arbitrary units. A fit is illustrated with the dashed line.

these simulations, the same behavior as in three dimensions can be observed with high-density regions between the plasma plumes and electric field generation. The value of the transverse electric field obtained in these simulations is illustrated for different transverse cell sizes in Fig. 3. It is illustrated in MV/m as a function of the mesh resolution, which is normalized to a transverse cell size of 18 μm, such that for a normalized mesh resolution of 1.5, the transverse cell size is 12 μm. For a transverse cell size of 12 μm (compared to 30 μm in three dimensions), the electric field can reach 2.6×10^8 V/m. As we can see, the value of the field increases as a function of the transverse resolution. A fit can be done (Fig. 3 dashed line) showing that a good convergence can be obtained and that with a transverse resolution of 4.5 μm, the electric field will reach almost 3.8×10^8 V/m. The dependency of the value of the electric field with the mesh resolution is here clearly demonstrated.

C. Proton radiography results

This electric field gives rise to a deflection of the protons passing between each pair of expanding plasma regions, which in turn results in a subsequent deficit in fluence on the proton radiographs. The experimental modulation of the proton dose $\delta n/n_p$ (with n_p being the homogenous dose) obtained on the detector for the gold hohlraum with Case A laser irradiation, Case B with a CH hohlraum driven, and the gold hohlraum with Case C are illustrated, respectively, in Figs. 4(a), 4(d), and 4(g). On each image darker means higher proton fluence (proton accumulation, compared to ballistic propagation with no deflection), and white means lower proton fluence (proton depletion).

From the experimental modulation of the proton dose on the detector $\delta n/n_p$, it is possible to infer the level of electric field responsible for the deflections observed in the experiment. Indeed, the proton dose is given by

$$\frac{\delta n}{n_p} \simeq \frac{-eD}{2\epsilon_P M} \int \nabla_\perp \cdot \boldsymbol{E}_\perp dx, \tag{2}$$

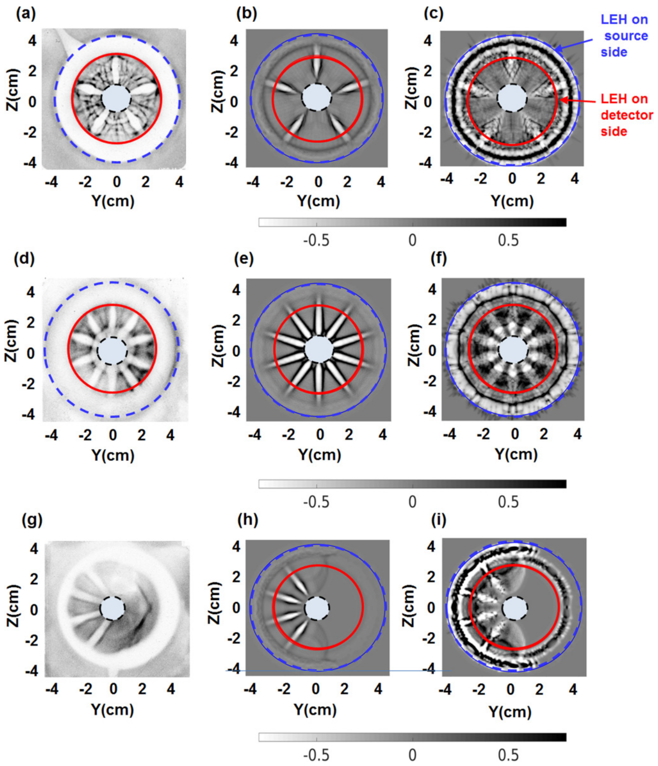

FIG. 4. Proton fluence $\delta n/n_p$ on the detector: experimental [(a), (d), and (g)], simulated with an electric field [(b), (e), and (h)], and with a magnetic field [(c), (f), and (i)]. Proton fluence [(a), (b), and (c)] for Case A, [(d), (e), and (f)] for Case B, and [(g), (h), and (i)] for Case C.

with D the distance between the target and the detector, e the electron charge, ϵ_p the proton energy, and M is the geometrical magnification. Because the electric field has nonzero values only over a characteristic distance L_x along hohlraum axis which is given as the longitudinal size of the bubble [$L_x \simeq 0.15$ cm, see Fig. 1(a)], the transverse electric field can be related to the proton dose by

$$|\nabla_\perp \cdot \boldsymbol{E}_\perp| = \frac{2\epsilon_P M}{eDL_x}\left|\frac{\delta n}{n_p}\right|. \tag{3}$$

For 14.7 MeV protons and a geometrical magnification corresponding to the position of the expanding plasma, we have $|\boldsymbol{E}_\perp|(\text{V/m}) \simeq 2 \times 10^{12} L_\perp(\text{cm})|\frac{\delta n}{n_p}|$. From the experimental modulations, we can infer that the typical size of the depletion area is close to $L_\perp \simeq 200$ μm for a proton depletion of $\delta n/n_p \simeq -0.8$. The electric field inferred from the experiments is close to 4×10^8 V/m, which is close to the asymptotic value of the electric field obtained from the 2D well-resolved simulations.

3D electric fields calculated from hydrodynamic quantities are given as input to a proton ray-tracing package, called ILZ [31], that creates a source and propagates protons with given energy through the electromagnetic field maps and deflects them according to the Lorentz force induced by the electromagnetic field using a classical particle pusher like those found in particle-in-cell (PIC) codes [32]. The finite source size of the backlighter has been taken into account in ILZ by a Monte Carlo treatment. The proton fluence on the detector is then reproduced by considering the dimensions and distances of the triplet source, object, and detector. Dose deposition of the protons on the detector is interpolated, also as done in the PIC method with Cloud-in-Cell techniques to enhance dynamic range. It is important to note that only by tracing the protons along their "line of slight" between the source and the film through the actual self-consistent fields obtained from a fully 3D simulations are we able to make valid comparisons to the experimental images.

The simulated proton fluence resulting from the coupling between Troll and ILZ for these three cases is illustrated in Figs. 4(b), 4(e), and 4(h). Because the electric field from 3D simulations is not fully converged, its value has been increased in order to match the experimental data, resulting approximately in an increase by a factor 10. In the gold hohlraum case, the protons were generated and sent through at $t = 1.3$ ns (0.8 ns for CH hohlraum). At this time, experiments show evidence of stagnation; however, the hydrodynamic simulations do not. Therefore we will compare only at early times, when the spatial structure resulting from deflection is clear and not dominated by stagnation, as observed at late times. Since the hohlraum is a simple cylinder, the red (solid) and blue (dashed) circles seen in the pictures correspond to the geometrical limitation induced by the length of the hohlraum [see Fig. 1(a)]. Outside the blue (dashed) circle the proton dose is homogeneous, and protons have a simple ballistic trajectory. Because ILZ does not describe scattering inside the matter, no comparisons can be made between the red (solid) and blue (dashed) circle. As we can see, only the presence of the electric field from the electron pressure gradient is enough to reproduce the unique structure observed in the experimental proton fluence: between each pair of plasma plumes, protons are deflected and pushed away, resulting in strong depletion between each pair and accumulation on the side.

Figures 4(a) and 4(b) show that for Case A the synthetic proton radiograph reveals a pattern of five areas of proton depletion consistent with the five laser focal spots [see Fig. 1(b)]. As shown in Figs. 4(g) and 4(h), while stagnation cannot be reproduced, the depletion of protons induced by a lateral electric field can be nicely reproduced. More importantly, it can be checked that the two plasma plumes without neighbors on one side (those at 7 and 11 o'clock) do not exhibit proton depletion. This can be explained by the lack of a high-electron density region (or lateral electric field) as seen in the hydrodynamic simulation in Fig. 2(a), which in turn leads to a lack of proton depletion in this area. Therefore, with this irradiation pattern, only four regions of protons depletion can be seen both in experiment and in the simulation.

Because the electric field at first order is the source of magnetic field, we can estimate the source term for the magnetic field as $\frac{\partial \boldsymbol{B}}{\partial t} = -\nabla \times \boldsymbol{E}$ and examine how the topology of B can act on protons. To estimate a given magnetic field as input in ILZ we assume a integration time of the source term of $t = 100$ ps and use the experimental or converged electric field (as discussed above). The case where the proton dose is the result of deflections due to this magnetic field is illustrated for the different cases A, B, and C, respectively, in Figs. 4(c), 4(f), and 4(i). Under the influence of this magnetic field, the protons now undergo some deflections between the plasma plumes that result in a "twist" motion and therefore in an accumulation between the plasma plumes. This results in protons not being completely ejected from between plumes, whereas the case of electric field alone [Figs. 4(b), 4(e), and 4(h)] more closely reproduces the observed feature of complete ejection.

III. CONCLUSION

In summary, this work represents a quantitative study of self-generated electric fields in hohlraums. The basis of the study is the direct comparison of experimental proton radiograph images to detailed 3D hydrodynamics simulations that are coupled to a proton ray-tracing simulation. Under several different irradiation patterns, the effects of self-generated electric and magnetic fields (due to the 3D structures occurring between the expanding plasma plumes) on protons passing through the hohlraum are analyzed. Peak values of E fields in these holraums are estimated to be $\sim 10^8$ V/m. It is found that electric fields are predominately responsible for the proton depletion between the plasma plumes (as seen in the experimental images), whereas the addition of a magnetic field tends to both expel and introduce proton flux into these depleted regions, something that is not seen in experimental images. On the other hand, a complete understanding of the B-field evolution would require a full magnetohydrodynamics description in order to simultaneously estimate the creation and convection of B fields. The results have important implications for understanding the role of electromagnetic fields in indirect drive ICF, not only in the understanding of the hohlraum physics, but also for generating HED plasma conditions in general.

ACKNOWLEDGEMENTS

The experiments were supported in part by the U.S. Department of Energy (DOE) (Grants No. DE-FG03-09NA29553, No. DE-SC0007168), LLE (No. 414090-G), NLUF (No. DE-NA0000877), and LLNL (No. B580243). This work was performed under the auspices of the DOE by Lawrence Livermore National Laboratory under Contract DE-AC52-07NA27344 and funded by the LLNL LDRD program under tracking code 17-ERD-039. S.C.W. acknowledges support from both the LLNL PRT program and CEA scientific exchange program.

---

[1] J. D. Lindl *et al.*, Phys. Plasmas **11**, 339 (2004).

[2] R. P. Drake, *High-Energy-Density Physics* (Springer, New York, 2006).

[3] B. A. Remington *et al.*, Science **284**, 1488 (1999).

[4] P. A. Amendt *et al.*, Plasma Phys. Control. Fusion **51**, 124048 (2009).

[5] S. I. Braginskii, *Review of Plasma Physics 1* (Consultants Bureau, New York, 1965).

[6] M. G. Haines, Phys. Rev. Lett. **78**, 254 (1997).

[7] J. A. Stamper, K. Papadopoulos, R. N. Sudan, S. O. Dean, E. A. McLean, and J. M. Dawson, Phys. Rev. Lett. **26**, 1012 (1971); J. A. Stamper and B. H. Ripin, *ibid.* **34**, 138 (1975); J. A. Stamper, E. A. McLean, and B. H. Ripin, *ibid.* **40**, 1177 (1978).

[8] D. W. Forslund, Geophys. Res. **75**, 17 (1970).

[9] W. Rozmus *et al.*, Plasma Phys. Control. Fusion **60**, 014004 (2018).

[10] A. J. McKinnon *et al.*, Rev. Sci. Instrum. **75**, 3531 (2004).

[11] L. Romagnani *et al.*, Phys. Rev. Lett. **95**, 195001 (2005).

[12] C. K. Li *et al.*, Rev. Sci. Instrum. **77**, 10E725 (2006).

[13] C. K. Li *et al.*, Phys. Rev. Lett. **97**, 135003 (2006).

[14] J. R. Rygg, F. H. Séguin, C. K. Li, J. A. Frenje, M. J.-E. Manuel, R. D. Petrasso, R. Betti, J. A. Delettrez, O. V. Gotchev, J. P. Knauer *et al.*, Science, **319**, 1223 (2008).

[15] C. K. Li, F. H. Séguin, J. R. Rygg, J. A. Frenje, M. Manuel, R. D. Petrasso, R. Betti, J. Delettrez, J. P. Knauer, F. Marshall *et al.*, Phys. Rev. Lett. **100**, 225001 (2008).

[16] C. K. Li *et al.*, Plasma Phys. Control. Fusion **51**, 014003 (2009).

[17] M. J.-E. Manuel, C. K. Li, F. H. Séguin, J. Frenje, D. T. Casey, R. D. Petrasso, S. X. Hu, R. Betti, J. D. Hager, D. D. Meyerhofer, and V. A. Smalyuk, Phys. Rev. Lett. **108**, 255006 (2012).

[18] C. K. Li, F. H. Séguin, J. A. Frenje, M. J. Rosenberg, H. G. Rinderknecht, A. B. Zylstra, R. D. Petrasso, P. A. Amendt, O. L. Landen, A. J. Mackinnon, R. P. J. Town, S. C. Wilks, R. Betti, D. D. Meyerhofer, J. M. Soures, J. Hund, J. D. Kilkenny, and A. Nikroo, Phys. Rev. Lett. **108**, 025001 (2012).

[19] C. K. Li *et al.*, Phys. Rev. Lett. **102**, 205001 (2009).

[20] C. K. Li *et al.*, Nucl. Fusion **53**, 073022 (2013)

[21] L. Lancia, B. Albertazzi, C. Boniface, A. Grisollet, R. Riquier, F. Chaland, K.-C. Le Thanh, P. Mellor, P. Antici, S. Buffechoux *et al.*, Phys. Rev. Lett. **113**, 235001 (2014).

[22] L. Gao *et al.*, Phys. Rev. Lett. **109**, 115001 (2012).

[23] C. K. Li *et al.*, Phys. Plasmas **16**, 056304 (2009).

[24] G. Sarri *et al.*, New J. Phys. **12**, 045006 (2010).

[25] M. Borghesi, G. Sarri, C. A. Cecchetti, I. Kourakis, D. Hoarty, R. M. Stevenson, S. James, C.D. Brown, P. Hobbs, J. Lockyear *et al.*, Laser Part. Beams **28**, 277 (2010).

[26] G. Sarri *et al.*, Phys. Rev. Lett. **106**, 095001 (2011).

[27] J. M. Soures *et al.*, Phys. Plasmas **3**, 2108 (1996).

[28] P-E. Masson-Laborde *et al.*, Phys. Plasmas **23**, 022703 (2016).

[29] E. Lefebvre *et al.*, Nucl. Fusion **59**, 032010 (2019).

[30] G. Shurtz *et al.*, Phys. Plasmas **7**, 4238 (2000).

[31] R. Riquier, Ph.D. thesis, Ecole Polytechnique and University of Paris-Saclay, 2016.

[32] C. K. Birdsall and A. B. Langdon, *Plasma Physics Via Computer Simulation* (Adam Hilger, IOP Publishing, Bristol, 1991).